Numerical Simulation of a Pump–Turbine Transient Load Following Process in Pump Mode

Giorgio Pavesi[1]
Department of Industrial Engineering,
University of Padova,
Via Venezia 1,
Padova 35131, Italy
e-mail: giorgio.pavesi@unipd.it

Giovanna Cavazzini
Department of Industrial Engineering,
University of Padova,
Via Venezia 1,
Padova 35131, Italy
e-mail: giovanna.cavazzini@unipd.it

Guido Ardizzon
Department of Industrial Engineering,
University of Padova,
Via Venezia 1,
Padova 35131, Italy
e-mail: guido.ardizzon@unipd.it

This paper presents the simulation of the dynamic behavior of variable speed pump–turbine. A power reduction scenario at constant wicket gate opening was numerically analyzed from 100% to 93% rpm corresponding to a power reduction from full load to about 70% with a ramp rate of 1.5% per second. The flow field analysis led to the onset and development of unsteady phenomena progressively evolving in an organized rotating partial stall during the pump power reduction. These phenomena were characterized by frequency and time–frequency analyses of several numerical signals (pressure, blade torque, and flow rate in blade passages). The unsteady pattern in return channel strengthened emphasizing its characteristic frequency with the rotational velocity decreasing reaching a maximum and then disappearing. At lower rotational speed, the flow field into the wickets gates channel starts to manifest a full three-dimensional (3D) flow structure. This disturbance was related to the boundary layer separation and stall, and it was noticed by a specific frequency. [DOI: 10.1115/1.4037988]

Introduction

World is faced with a complex and challenging restructuring of its energy system. Many countries have agreed to undertake major cuts in its greenhouse gas emissions and to increase power generation from renewable resources, experiencing an increased power production from intermittent sources such as small hydropower, wind power, and photovoltaics power plants.

Renewable energy is extremely variable, and a large share of it is a challenge for the stability of the transmission system, as well as security of supply for the consumers. There is a need for back up capacity to generate power during high demand, as well as a need for storage capacity for surplus power.

Pump–turbine units have become nowadays an interesting way to increase stability of electrical power networks due to their high level of operating flexibility. The main applications of pumped storage are load shifting, price arbitrage, primary and secondary reserves, peak power supply, grid congestion avoidance, load following, and for supporting variable electricity generation [1]. Moreover, according to Joint Research Centre EU [2], pumped hydropower storage is currently the only widespread electricity storage technology able to offer the large-scale storage that is needed for accommodating renewable electricity under the 2020 EU energy targets [3].

The traditional pump–turbine equipment design is the reversible single-stage Francis pump–turbine, which acts as a pump in one direction and as a turbine in the other. On a conventional unit, pumping occurs at a fixed speed and almost fixed wicket gate opening. The power input is nearly constant at the input rating of the pump, and the discharge varies with the pumping head. Although this technology is proven and has worked well for over six decades, there are limitations to its performance. Adjustable-speed machines enable the power consumed in the pumping mode to be varied over a range of outputs.

Consistently, an adjustable speed-pumping unit can operate over a larger head range and pumping power input range than a single speed unit and offer several advantages for both pumping and generating modes [4–9] such as:

(a) possibility of active power control in pumping mode
(b) efficiency increase and wide range of operation in generating mode especially under partial load
(c) network stability improvement by reactive power control
(d) network stability improvement by instantaneous active power injection in the grid (flywheel effect)

This flexibility is frequently employed by adjusting the speed of units during light load periods over a load range of 50–60% of rated pumping power. This means that a unit does not have to wait until a block of power equal to its full pump capacity rating is available before pumping can begin. Thus, there are more opportunities to purchase blocks of pumping power enabling more real-time response to grid conditions [10].

In that context, it is requested to develop pump–turbines that reliably stand dynamic operation modes, fast changes of the discharge rate, and with stability limits positioned considerably away from the normal operating range.

At off-design conditions, the wickets gates channel and the draft tube do not work properly and give awkward boundary conditions to the impeller, together with a strong fluid-dynamical interaction between rotor and stator parts [11–15]. The flow features such as separation and recirculation occur severely in an unsteady manner. Nonrotating components of the turbine, such as guide vanes, stay vanes, head cover, draft tube cone, and also on the hydraulic system, especially the penstock may experience strong dynamic load and high-cycle fatigue stress that may result in the propagation of cracks and the failure of the shear pin or the guide vanes stem.

Frequency and time–frequency experimental analyses highlighted the existence of rotating structures of pressure pulsations at the impeller exit appearing and disappearing in time, having greater intensity at part loads [16–20]. This strong rotor–stator interaction resulted to be further emphasized in multistage pump–turbines in which a "full-load-instability" develops in the range from 60% to 90% of the design flow rate [19] and quite independent to the rotational speed [17].

Recently, Deyou et al. [21] focused the numerical analyses into the hump region trying to correlate the hump characteristics to the vortex motion in the tandem cascade.

[1]Corresponding author.

Contributed by the Fluids Engineering Division of ASME for publication in the Journal of Fluids Engineering. Manuscript received September 13, 2016; final manuscript received July 18, 2017; published online November 3, 2017. Assoc. Editor: Olivier Coutier-Delgosha.

Numerical analyses were also carried out by Gentner et al. [22] and Cavazzini et al. [23] highlighting the dependence of the flow behavior in the head drop from a perturbation of the wickets gates channel flow field, characterized by an unsteady flow rate migrations between passages and by unsteady flow jets.

The results at constant flow rate of both experimental and numerical analyses highlighted the existence of a spatial fluctuation pattern concentrated close to the impeller exit, whose fluctuations levels increase at off-design conditions.

Even though these studies have allowed to obtain interesting information on the unstable behavior of pump–turbines, to solve instability problems, and to enlarge the working range of pump–turbine significantly, an in-depth understanding of the unsteady flow mechanism during power regulation is crucial for the production stabilization.

In this context, time domain simulation of the dynamic behavior of the pump–turbine can provide useful insights for decision-making.

The aim of this investigation was to analyze the development of the unsteady phenomena of a reversible pump–turbine operating in pump-mode load following control function. The numerical analysis included the dynamic pressure measurements from best efficiency point (BEP) to part flow rate at a fixed gradient of the power reduction. The analysis of pressure fluctuations was conducted in both frequency and time frequency domains.

A three-dimensional (3D) transient flow simulation in the entire pump–turbine was conducted to investigate the rotor–stator interaction by adopting the detached eddy simulation turbulence model. A commercial computational fluid dynamics program was utilized to study the flow through this pump–turbine in its stationary and transient passages, from 100% optimum load to 70% of part load reduction by an adjustable-speed approach.

Numerical Model

Numerical analyses were carried out by the commercial software ANSYS 15.0 on the first stage of a two stage reversible pump–turbine in pump-operating mode (Fig. 1). Table 1 reports the main geometrical data of the considered pump–turbine. In the analyzed configuration, the radial gap between the trailing edge of the guide vanes and the impeller tip was 10.5 mm, which is 5.25% of the impeller radius. The relative azimuthal position of the guide vanes was fixed by rotating the whole guide vane system from the face-to-face configuration ($\lambda = 0$ deg) to the configuration with the azimuthal position of the guide vanes $+8$ deg out of alignment (Fig. 2).

Moreover, Fig. 2 shows that some of the midheight points were the unsteady pressure was recorded during the numerical analysis.

The numerical model of the entire machine included inlet duct, return channel, wicket vanes, impeller, and leakage system.

Table 1 Geometry characteristics, position of each interface (hatched curves), and performance parameters of the tested pump–turbine

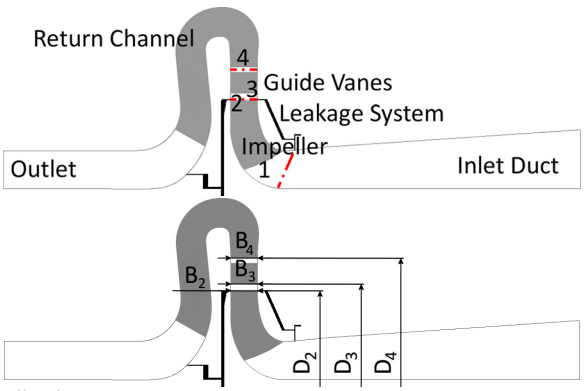

Impeller data				
D_2 (mm)	B_2 (mm)	n_b	β_{2b} (deg)	ϕ_{BEP}
400	40	7	26.5	0.125
Guide vanes data				
D_3 (mm)	B_3 (mm)	n_{bW}	α_{3b} (deg)	λ (deg)
410	40	22	10–30	−8 to 8
Return channel vanes data				
D_4 (mm)	B_4 (mm)	n_{bR}	α_{4b} (deg)	
516	40	11	30	

A sensitivity study taking into account six levels of mesh refinement was carried out to evaluate the influence of the mesh density on the simulation results. Figure 3 presents the head computed at BEP conditions for the different mesh densities.

The stage head H was evaluated in preliminary tests to assure grid independent solution for the impeller and to guarantee the capacity of numerical solution to capture the local pressure pulsations as well. Even if the sensitivity analysis highlighted a grid independent solution with about 200,000 elements per impeller passage, the intensity and the extent of the local pressure pulsations appeared to be correctly evaluated only with grid greater than 300,000 elements per passage. To be sure of the capacity of the numerical solution to capture local pressure pulsations in the whole domain, as a precautionary measure, the adopted number of elements was further increased to 565,000. The resulting impeller computational domain that was used had 3.96×10^6 of cells, an O grid was performed, and $y+$ values below 15. The draft tube was discretized by a structured mesh of about 339,500 elements with a $y+$ values lower than 20. O-type grids were adopted for both the wicket gate and the return channel discretization. Following the same philosophy used for the impeller, the number of elements

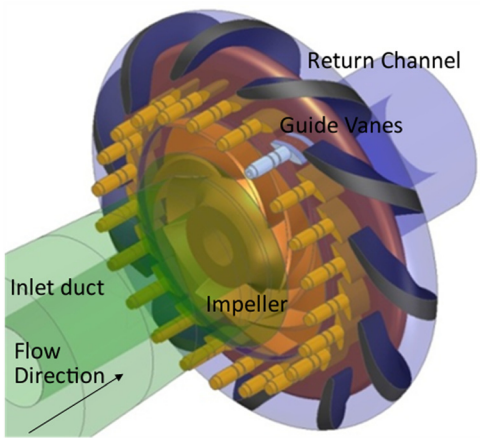

Fig. 1 3D scheme of the tested configuration

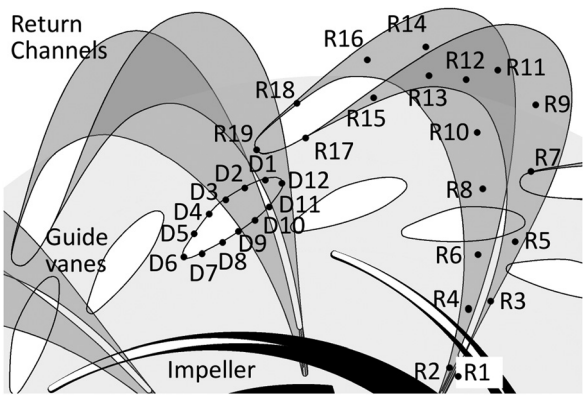

Fig. 2 Detail and sketch of the tested configuration ($\lambda = 8$ deg) with the distribution of monitor points

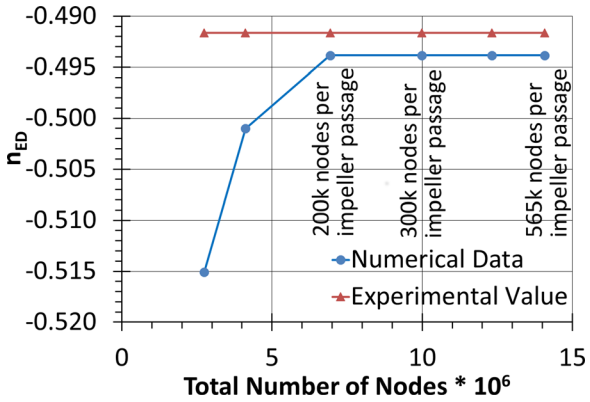

Fig. 3 Comparison of simulated and experimental discharge factor n_{ED} at BEP condition for different mesh densities

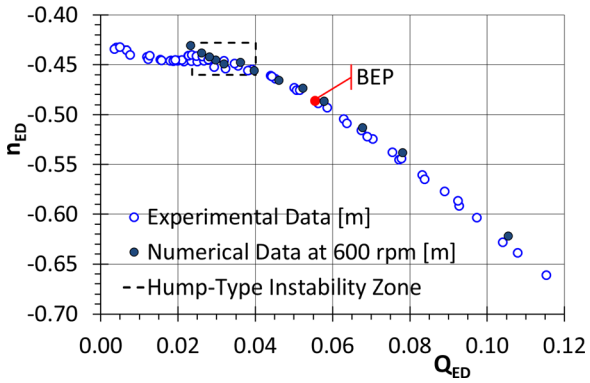

Fig. 4 Comparison between numerical and experimental head curves

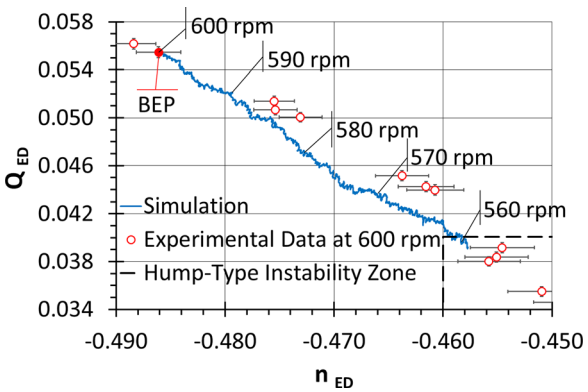

Fig. 5 Numerical dimensionless discharge–speed curve

was increased to about 4.3×10^6 and 5.4×10^6 of cells, respectively. The leakage from the labyrinth seal was also considered, and several H-blocks were built to describe the cavities. The final mesh specifications are summarized in Table 2.

The choice of the turbulence model is a key issue in computational fluid dynamics. According to the large flow separations expected at part load, a detached eddy simulation model was adopted. On both blades and end walls, the boundary layer was assumed fully turbulent with an automatic near-wall treatment, which automatically switches from a low-Re formulation to wall functions based on the grid spacing.

All the interfaces between stator–rotor blocks were standard transient sliding interfaces.

At the inlet boundary condition, the total pressure was imposed with the values taken from the experimental data and a turbulence intensity of the 5%. At the outlet, due to the highly disturbed flow field, an opening condition with entrainment option, an average static pressure, and a zero gradient of the turbulence was fixed. The boundary was located at 2.3 hydraulic diameters downstream the return vane trailing edge.

The power reduction was simulated by a time-varying boundary condition in which the impeller was slow down from 100% to 93% rpm corresponding from full load to about 70% of the full load with a power ramp rate of 1.5% per second.

A second-order implicit time stepping was adopted for the time discretization and a time step of 1 deg. The root mean square Courant number resulted to be lower than 1.9 for all the power, guaranteeing an accurate resolution of the transient details. The maximum resulting root-mean-square values for the residuals were u momentum 10^{-4}, v momentum 10^{-4}, w momentum 3×10^{-5}, and turbulence kinetic energy 10^{-4}.

Results

Validation of Numerical Model at Constant Flow rate Conditions. To validate the numerical model, the numerical head curve was compared with that experimentally acquired on the pump–turbine under test according to ISO standards.

Numerical analyses were carried out for some operating points at a constant rotation rate of 600 rpm. The numerical data were acquired for five impeller revolutions after more than 20 revolutions required to achieve a quasi-steady simulation convergence. The comparison in terms of head is reported in Fig. 4. The agreement between average numerical and experimental results is good with an error smaller than 2% near the best efficiency point and smaller than about 4% at partial loads (Fig. 4).

The good agreement in terms of mean values between numerical and experimental results demonstrated the capability of the numerical model to predict the performance of the pump–turbine with sufficient accuracy not only at BEP condition.

Numerical Analysis of the Pump–Turbine in a Power Reduction Scenario. To study the evolution of the flow field in a dynamic power reduction scenario, the wicket vane was fixed at 18 deg and kept constant during the simulation.

The transient numerical simulation on the entire machine was carried out with a time-varying boundary condition in which the impeller speed was reduced every time step, whereas the total pressure at inlet and the average static pressure at outlet were maintained constant.

In this case, a simple linear variation of the impeller speed from 100% to 93% was fixed.

The initialization was based on the results of the steady simulation carried out for the BEP flow rate.

Figure 5 reports the dimensionless factors during power reduction. The pump flow rate decreased progressively with limited oscillations only at lower impeller speed (Fig. 5). The flow field

Table 2 Pump mesh specifications used

	Inlet duct	Impeller blade	Guide vanes	Return channels	Labyrinth seal	Total
Type of elements	Hexahedra	Hexahedra	Hexahedra	Hexahedra	Hexahedra	
Number of elements	554,880	3,737,676	3,951,491	5,177,764	795,843	14,217,654
Max $y+$	15	20	22	25	97	

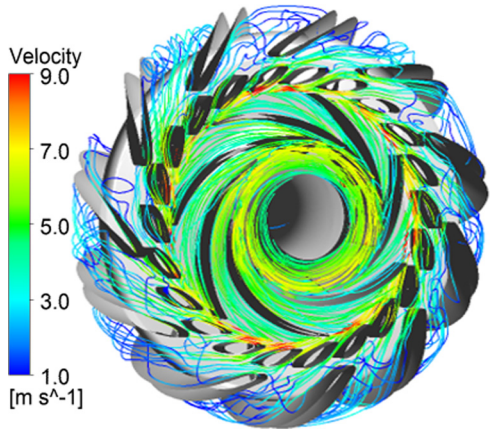

Fig. 6 Flow field inside the pump–turbine for $n_{ED} = -0.458$

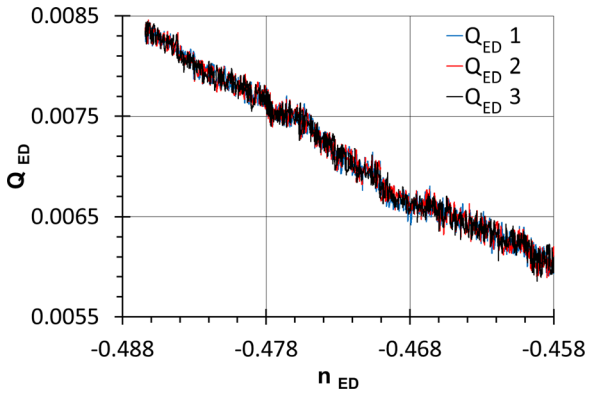

Fig. 7 Numerical dimensionless discharge–speed curves of three consecutive impeller channels

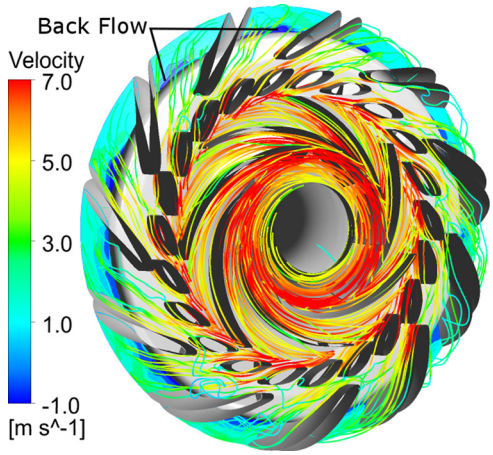

Fig. 8 Flow field inside the pump–turbine for $n_{ED} = -0.482$

inside the impeller did not show instabilities up to the lower speed factor (Fig. 6), and consistently, the flow rate inside in each impeller channel showed the same progressive and regular flow reduction highlighted for the pump (Fig. 7).

In the return channel, the flow field was perturbed by a sort of unsteady stall phenomena from the very beginning of the simulation with channels characterized by vortexes partially blocking the channels (Fig. 8) and forcing the streamlines to climb over the reverse flow volume present in the corner between the vane suction side and the U-turn hub.

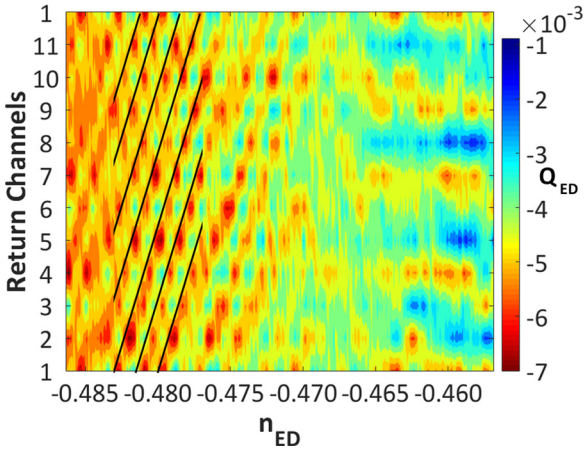

Fig. 9 Numerical dimensionless discharge–speed in the return channels

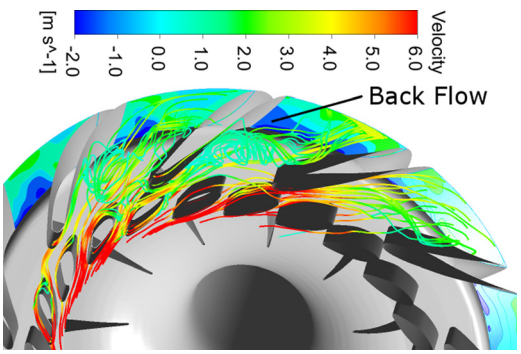

Fig. 10 Flow field inside the pump–turbine for $n_{ED} = -0.482$

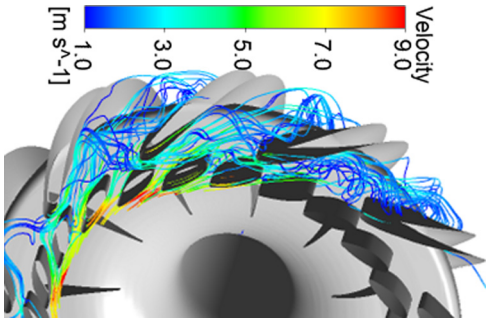

Fig. 11 Flow field inside the pump–turbine for $n_{ED} = -0.472$

The blockage action was confirmed by the analysis of the flow rate passing through the return channels (Fig. 9). Each return channel alternated between partially blocked and unblocked flow.

During the power reduction, the perturbation of the pump–turbine flow field evolves in a rotating partial stall of five cells moving from one channel to the subsequent one according to the impeller rotation direction, as highlighted in Fig. 9 by the black lines.

The progressive decrease of the flow rate causes, in the first phase, the development and enlargement of the regions of flow separation (Fig. 10) and an increase of the flow rate oscillation (Fig. 9).

Successively, the organized partial stall lost the coherence, the stall breaks up progressively, and the vortexes involve quite uniformly all the channels (Figs. 9 and 11).

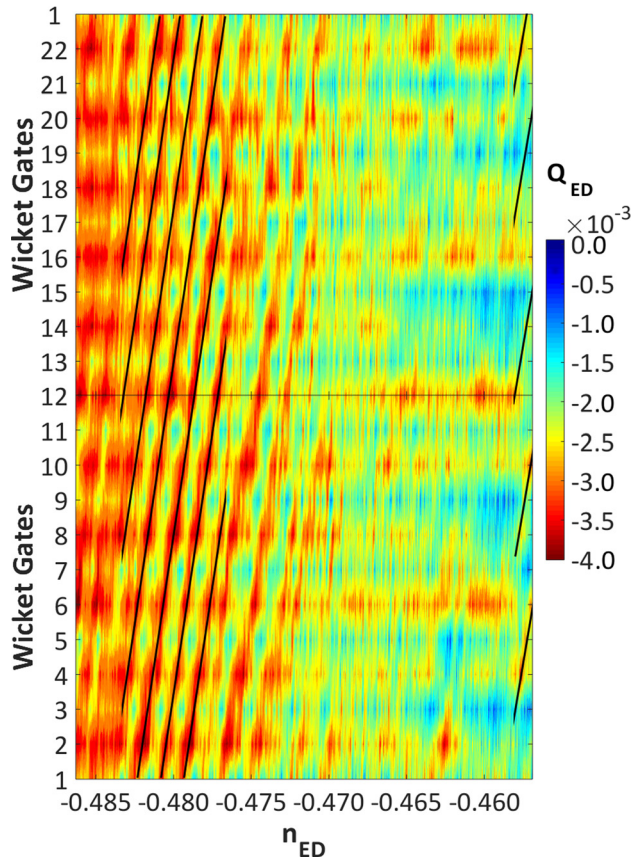

Fig. 12 Numerical dimensionless discharge–speed curves of the wicket gates

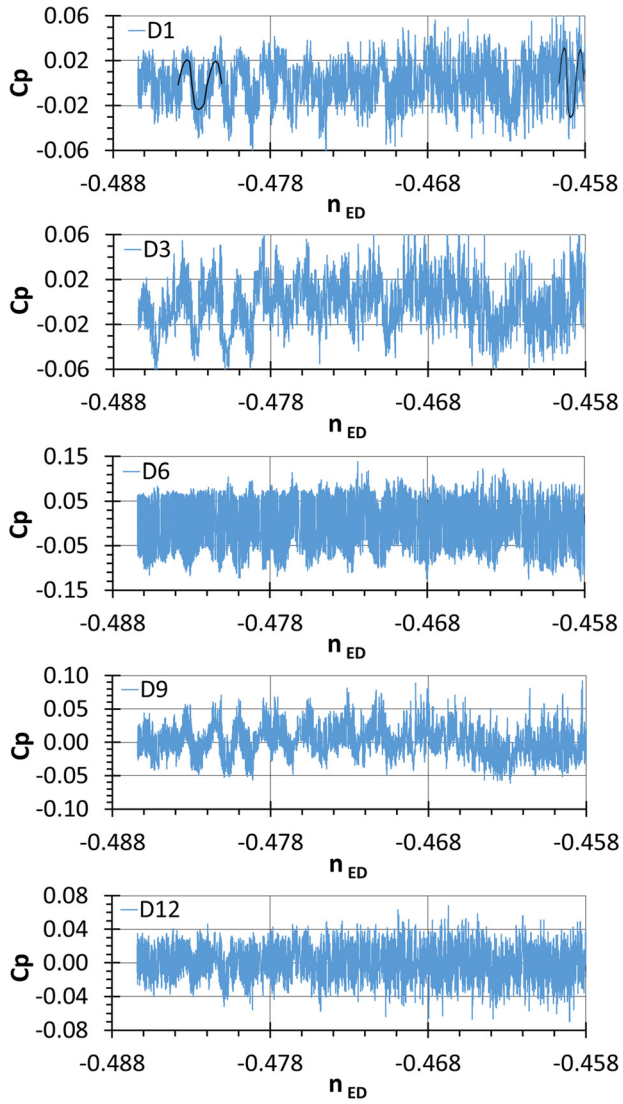

Fig. 13 Pressure coefficient versus speed factor acquired in the wicket gate

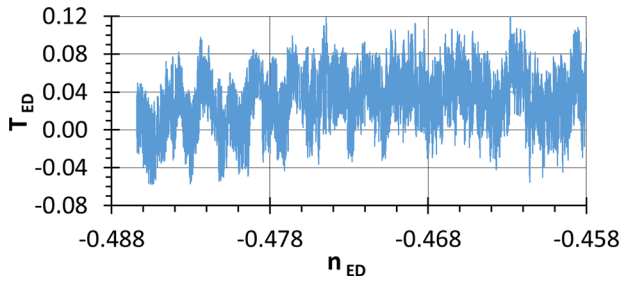

Fig. 14 Wicket gate torque factor versus speed factor

At higher-speed factors ($-0.482 \lesssim n_{ED} \lesssim -0.478$), the wicket gate channels experience flow rate oscillation (Fig. 12), and 11 channels with low flow rate are alternated by 11 channels with higher flow rate.

Close to the hump zone, the blockage action involves two or three adjacent wicket gate channels (Fig. 12 $n_{ED} \gtrsim -0.462$), and the flow field evolves in a rotating partial stall of cells moving from one group of channels to the subsequent one according to the impeller rotation direction, as highlighted in Fig. 12 by black lines.

Due to the rotating characteristics of the blocking cells, the vanes were characterized by time fluctuations of the pressure distributions and hence of the torque, depending on the evolution of the flow field around the blade. Figure 13 reports the evolution of the pressure coefficient on five of the monitor points marked on the wicket gate of Fig. 2, while Fig. 14 shows the torque factor over time on a wicket gate during power reduction.

The history of the signals highlights two phases; in the first, up to about $n_{ED} = -0.475$, low frequencies are more evident than in the second phase. Moreover, the pressure coefficient and the torque fluctuations on the blades increase in peak-to-peak amplitude with the impeller speed reduction, as highlighted by the black lines in Fig. 13.

The development of these unsteady phenomena in the stators affected the pressure distribution on the vanes, thereby modifying their load distribution and induces dynamic load on the shear pin or the guide vanes stem.

Time–Frequency Characterization of the Unstable Behavior. Spectral analyses in frequency and in time–frequency domain were carried out to characterize the unsteady phenomena identified in the previous flow field analysis [16].

The frequency content of the numerical signals, acquired at each time step during the whole simulation of power reduction, was determined by using a Hamming window in the Lomb periodogram.

Figure 15 reports the power spectrum of the flow rate signal acquired in the return channel.

The spectrum is dominated by peaks at low frequency ($St < 0.1$), whose amplitude is greater than that of the blade passage frequency (BPF) ($St \cong 1$).

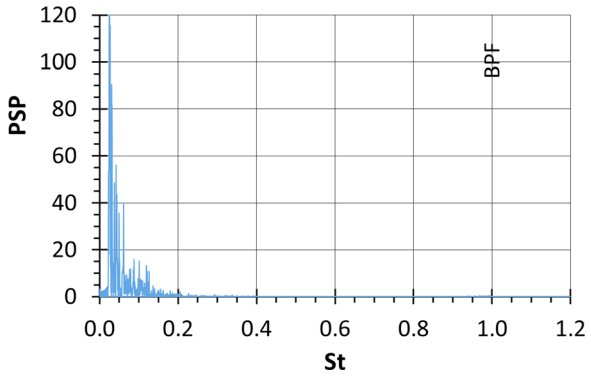

Fig. 15 Normalized power-spectra of the discharge factor acquired in the return channels 2 of Fig. 2

The signal processing in the frequency domain makes it possible to analyze the spectral components contained in a signal, but it does not make assigning these spectral components to time feasible. In order to identify the instant and hence the operating condition in which the frequency characterizing the rotating block appears, a time frequency characterization was performed via wavelet transform analysis.

For all the series of data, the continuous wavelet transform $W(s, n)$ was computed via the FFT-based fast convolution according to the following equation:

$$W(s,n^*) = \sum_{k=0}^{N-1} X_k \left(\sqrt{\frac{2\pi s}{\delta t}} \psi_0^*(s\omega_k) e^{i\omega_k n^* \delta t} \right) \quad (1)$$

where X_k is the discrete Fourier transform of the discrete sampled signal x_n, k is a frequency index, N is the length of the data series, s is the wavelet scale, δt is the sampling interval, and n^* is the localized time index. $\psi_0^*(s\omega_k)$ is the complex conjugate of the Fourier transform of the scaled version of the "mother wavelet" $\psi(t)$, and ω_k is the angular frequency (note that if $k \leq N/2$, $\omega_k = 2\pi k/N\delta t$; else $\omega_k = -2\pi k/N\delta t$). The normalization factor was introduced to obtain a unit energy at each scale. As regards the choice of the mother wavelet, in this case, a complex Morlet wavelet with $2\pi f_0 = 8$ was chosen.

Figure 16 reports the continuous wavelet transform of the signals of the flow rate passing through the return channels 2.

The frequency, corresponding to the flow variation, is clearly identifiable and starts to appear from nearly the BEP flow rate (Figs. 9 and 16). The intensity of the flow variation reached a maximum after about a power reduction of the 11%. With further

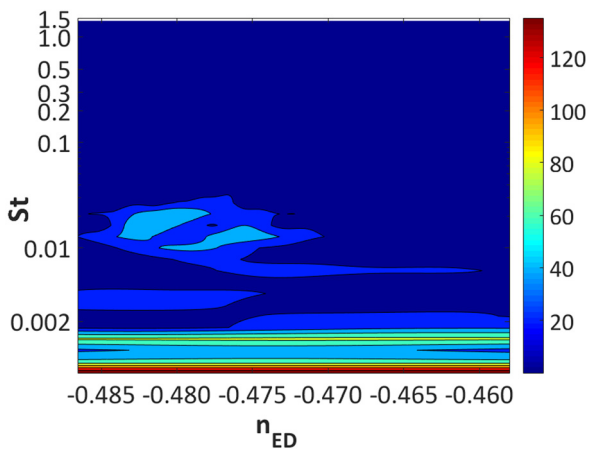

Fig. 16 Normalized power-spectra of the discharge factor acquired in the return channels 2 of Fig. 2

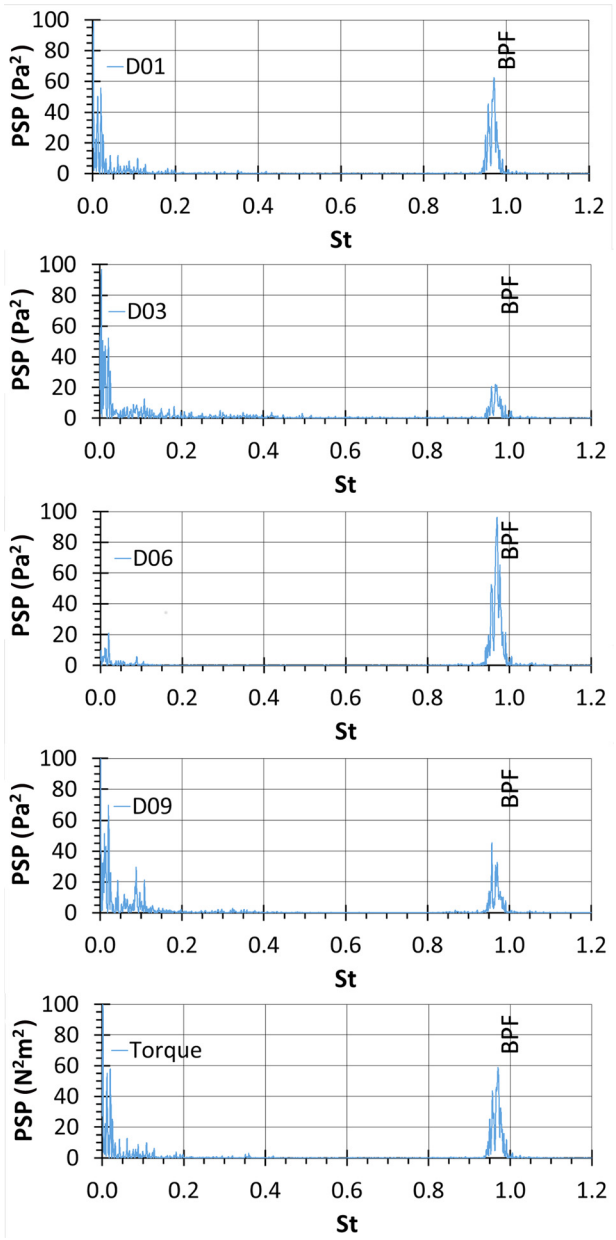

Fig. 17 Normalized power-spectra of pressure and torque signal acquired on the wicket gate

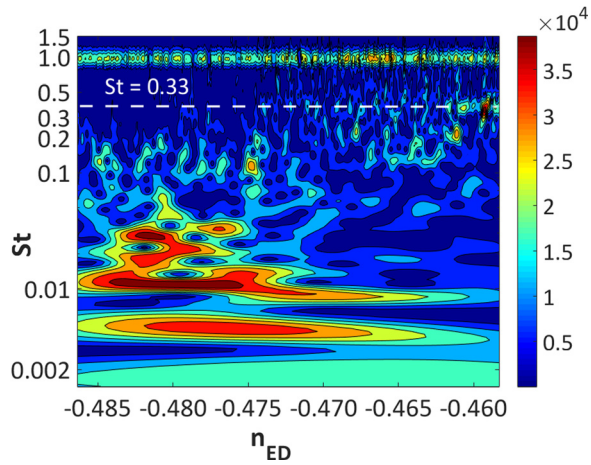

Fig. 18 Normalized power-spectra of pressure signal acquired in the wicket gate monitor point *D*12 of Fig. 2

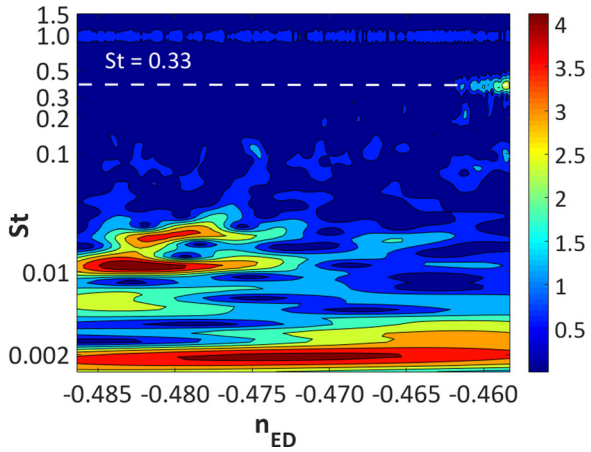

Fig. 19 Normalized power-spectra of torque signal of a wicket gate

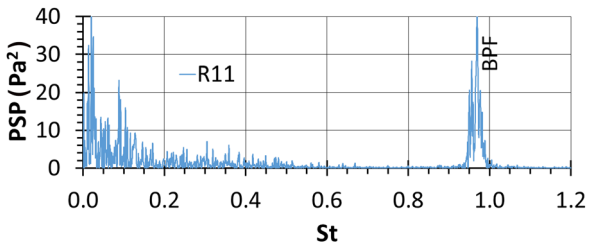

Fig. 20 Normalized power-spectra of pressure signal acquired on the wicket gate

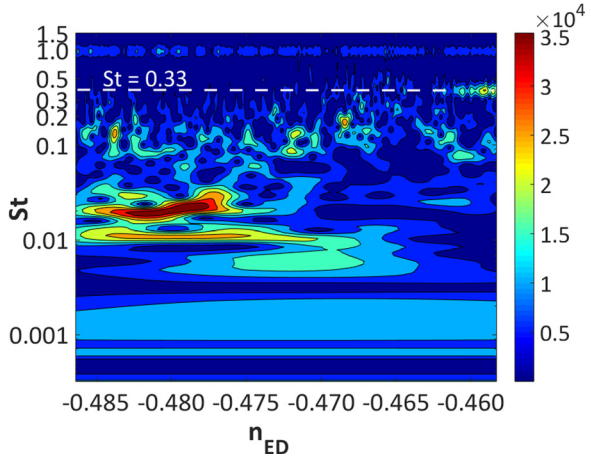

Fig. 21 Normalized power-spectra of pressure signal acquired in the return channel monitor point *R*11 of Fig. 2

reduction of the impeller rotational speed, the flow field perturbation into the pump–turbine evolves, and the organized rotating stall disappears at a speed factor value of about $n_{ED} = -0.475$ replaced by a flow fluctuation dominated by a very low frequency ($St \leq 0.01$).

The BPF is weakly appearing in the spectrum consistently with the uniform and regular flow field into the impeller.

These remarks are confirmed by the normalized power-spectra of pressure and continuous wavelet transforms calculated for the signals acquired in the stator domains, some of which are reported from Figs. 17–21.

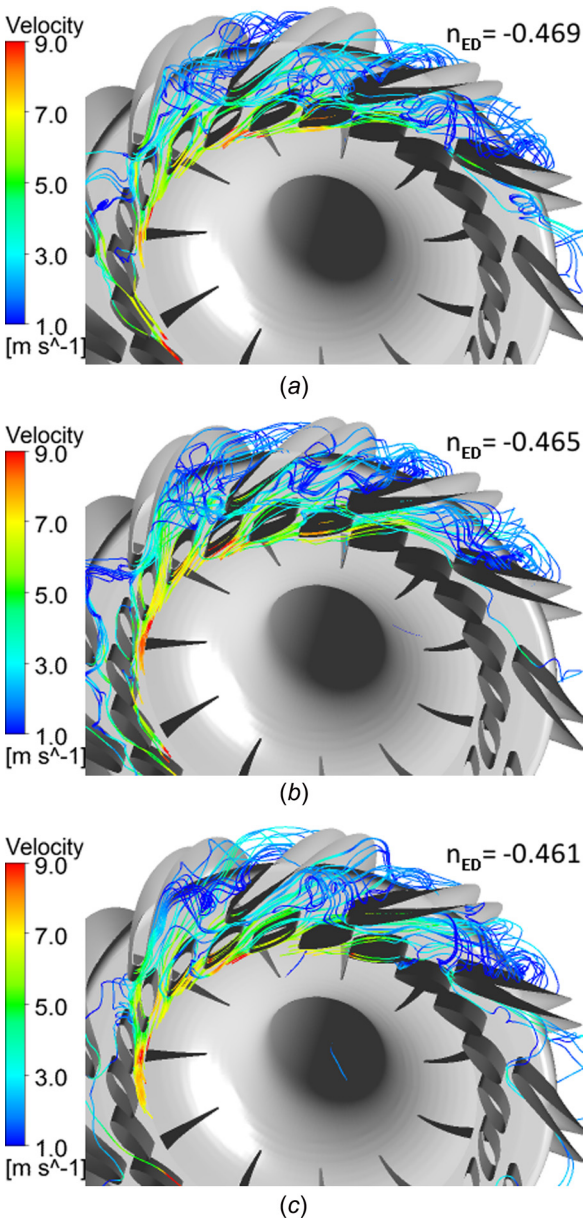

Fig. 22 Flow field inside the pump–turbine at different speed factors

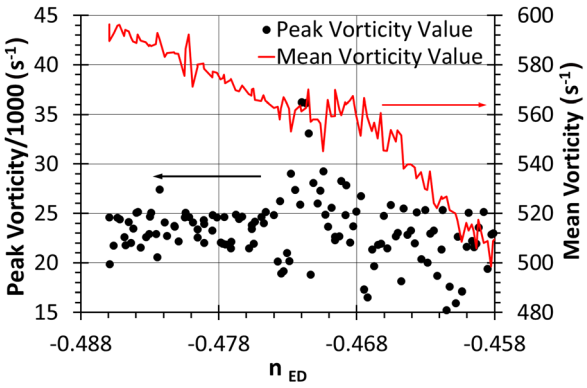

Fig. 23 Maximum and mean vorticity values ($\nabla \times V$) evaluated in the return channel subdomain versus different speed factors

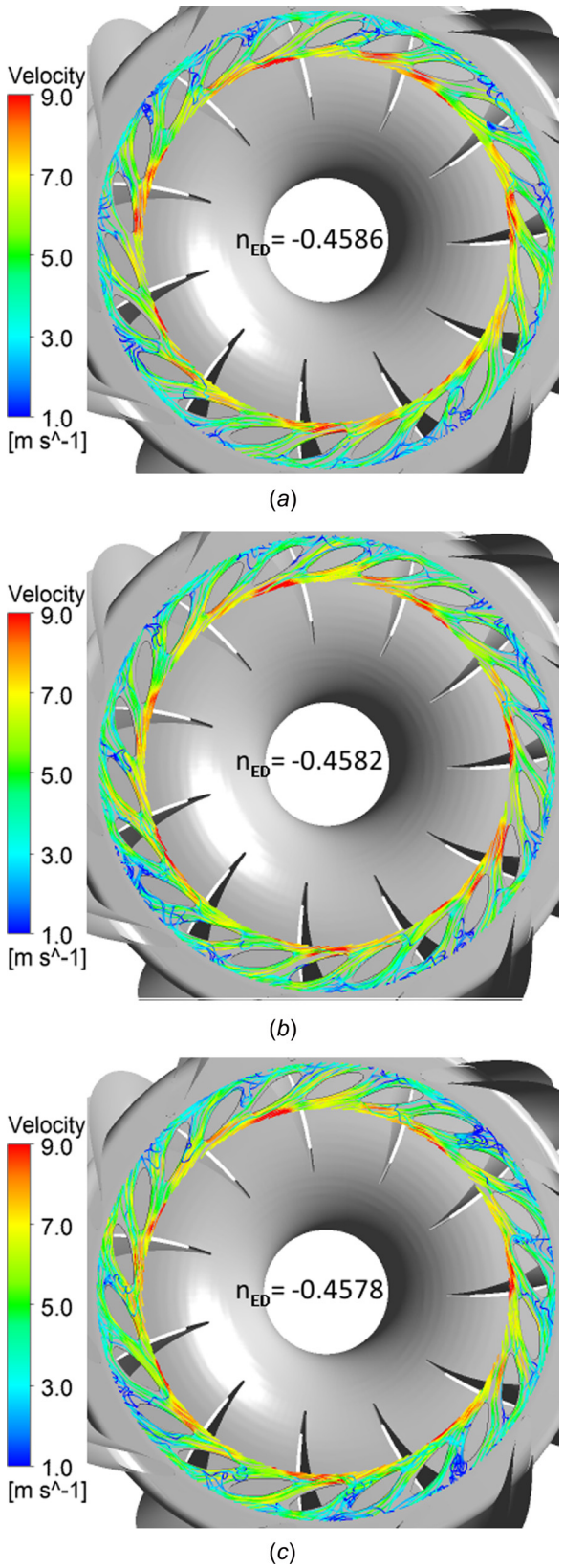

Fig. 24 Flow field inside the wicket gates at different speed factors

The blade passage frequency is captured, with more or less intensity during the whole load rejection simulation, in the frequency and time frequency transforms of the signals of the static pressure and of the torque acting on the wicket vanes (Figs. 17–21).

At the wicket blade leading edges, due to the proximity of the impeller outlet, the pressure pulsation, caused by the rotation of the impeller blades, is strongly perceived by the guide vanes, dominating the resulting power spectrum (Fig. 17). Vice versa, the spectral characterization of the sections far from the impeller demonstrates a relationship between the appearance of a well-defined frequency in the spectral content of the machine and the fluid-dynamical evolution of the unsteady phenomena during the power reduction.

First, the perturbation of the pump–turbine flow field evolves in an organized rotating partial stall. This instability induces lobs of pressure fluctuations and dynamic load on the shear pin or the guide vanes stem.

Successively, the back flow volumes in the return vane channels become quite stable. The flow rate tends to remain quite constant in all the return channels (Fig. 9), and the flow path does not change evidently (Fig. 22). The analyses show vortices witch intensity and structure changed to a limited extent for speed factors lower than −0.468, as highlighted in Fig. 23.

Consistently, the stator elements experience a phase of limited dynamic loads or actions as Figs. 18, 19, and 21 highlighted into the speed factor range −0.468 to −0.460.

A further reduction of the impeller speed forces the pump to work close to the hump zone (Fig. 4).

Figure 24 presents the streamlines evolution into each wicket gate channel during impeller revolutions.

The nuclei were not stable, and when they appeared the time frequency analyses highlighted the start-up of pressure and torque oscillations at a frequency close to St = 0.33 (Figs. 18–20).

This unsteadiness is in agreement with the evolution a full three-dimensional flow structure into the wickets gates channel visualized experimentally [24,25] in the hump zone.

Conclusions

Numerical analyses were carried out on a low specific speed pump–turbine, operating at full and part load conditions on pump mode. The pressure and the torque variation in time and frequency domains were used to analyze the flow field when the impeller was slow down from 100% to 93% rpm corresponding to a power reduction from full load to about 70% with a ramp rate of 1.5%.

The different unsteady patterns were highlighted coherently by both spectral and bispectral analysis of the pressure data.

When the flow rate decreased below the BEP flow rate, stall cells, partially blocking the regular flow, moves from one channel to the subsequent one in the impeller rotation direction with increasing intensity during the load rejection. Each impeller channel alternates partial blocked flow according to the rotation frequency of the stall cell. The unsteady pattern in return channel strengthened emphasizing its characteristic frequency with the rotational velocity decreasing reaching a maximum and then disappearing.

For lower rotational speed, the periodic back flow inside the return channel disappeared. The path analyses show only vortices with intensity and structure changed stochastically.

At lower rotational speed, the flow field into the wickets gates channel starts to manifest a full three-dimensional flow structure. This disturbance was related to the boundary layer separation and stall was noticed with a frequency very close to St ≈ 0.335 identified by experimental measured.

Nomenclature

B = impeller or guide vane or return channel width (m)
$\mathrm{BPF} = n_b n/60$ = blade passage frequency (Hz)
$c_p = (p - \bar{p})/(\rho(\omega(D_2/2))^2)$ = pressure coefficient
D = diameter (m)
g = gravitational acceleration (m s^{-2})
Gxx = power-spectra ()^2

H = head (m)
n = rotational speed of the impeller (rpm)
n_b = impeller number of blades
n_{bR} = return vane number of blades
n_{bW} = wicket guide number of blades
$n_{ED} = (nD_2)/\sqrt{gH}$ = speed factor
p = pressure (Pa)
$\bar{p}$ = pressure averaged along the time (Pa)
Q = flow rate ($m^3\ s^{-1}$)
$Q_{ED} = Q/(D_2^2\sqrt{gH})$ = discharge factor
$St = f/BPF_{Des}$ = Strouhal number
$T_{ED} = T/(\rho D_2^3 gH)$ = torque factor
V = velocity ($m\ s^{-1}$)
α = angle (deg)
β = angle (deg)
∇ = del operator
λ = guide vanes' azimuthally position (deg)
ω = angular rotational velocity (rad s^{-1})

Subscripts

b = blade
Des = design rotational speed of the impeller
2 = outlet impeller
3 = inlet wicket gate
4 = inlet return channel

References

[1] SET-Plan Information System (SETIS), 2011, "Electricity Storage in the Power Sector: Technology Information Sheet," JRC European Commission, Luxembourg, The Netherlands, accessed Sept. 30, 2017, https://setis.ec.europa.eu/related-jrc-activities/jrc-setis-reports/electricity-storage-power-sector-technology-information

[2] Arantegui, R., Fitzgerald, N., and Leahy, P., 2012, "Pumped-Hydro Energy Storage: Potential for Transformation From Single Dams," JRC European Commission, Luxembourg, The Netherlands, accessed Sept. 30, 2017, https://setis.ec.europa.eu/sites/default/files/reports/Pumped-hydro-energy-storage-potential-for- transformation-from-single-dams.pdf

[3] European Union, 2009, "Directive 2009/28/EC of the European Parliament and of the Council on the Promotion of the Use of Energy From Renewable Sources and Amending and Subsequently Repealing Directives 2001/77/EC and 2003/30/EC," European Union, Brussels, Belgium, accessed Sept. 30, 2017, http://eur-lex.europa.eu/legal-content/EN/ALL/?uri=CELEX:32009L0028

[4] Grotenburg, K., Koch, F., Erlich, I., and Bachmann, U., 2001, "Modelling and Dynamic Simulation of Variable Speed Pump Storage Unit Incorporated Into the German Electric Power System," European Conference on Power Electronics and Applications (EPE), Graz, Austria, Aug. 27–29, pp. 1–10.

[5] Hodder, A., 2004, "Double-Fed Asynchronous Motor-Generator Equipped With a 3-Level VSI Cascade," Ph.D. thesis, École Polytechnique Fédérale de Lausanne, Lausanne, Switzerland.

[6] Kopf, E., Brausewetter, S., Giese, M., and Moser, F., 2004, "Optimized Control Strategies for Variable Speed Machines," 22nd IAHR Symposium on Hydraulic Machinery and Systems, Stockholm, Sweden, June 29–July 2, pp. 1–9.

[7] Kuwabara, T., Shibuya, A., Furuta, H., Kita, E., and Mitsuhashi, K., 1996, "Design and Dynamic Response Characteristics of 400 MW Adjustable Speed Pumped Storage Unit for Ohkawachi Power Station," IEEE Trans. Energy Convers., **11**(2), pp. 376–384.

[8] Schwery, A., Fass, E., Henry, J.-M., Bach, W., and Mirzaian, A., 2005, "Pump Storage Power Plants, ALSTOM's Long Experience and Technological Innovation," HYDRO, Villach, Austria, Oct. 17–20, pp. 1–10.

[9] Simond, J. J., Sapin, A., and Schafer, D., 1999, "Expected Benefits of Adjustable Speed Pumped Storage in the European Network," Hydropower into the Next Century, Gmunden, Austria, pp. 579–585.

[10] Henry, J. M., Houdeline, J. B., Ruiz, S., and Kunz, T., 2012, "How Reversible Pump-Turbines Can Support Grid Variability—The Variable Speed Approach," HYDRO Innovative Approaches to Global Challenges, Bilbao, Spain, Oct. 29–31, pp. 1–10.

[11] Sun, Y., Zuo, Z., Liu, S., Liu, J., and Wu, Y., 2014, "Distribution of Pressure Fluctuations in a Prototype Pump Turbine at Pump Mode," Adv. Mech. Eng., **2014**, p. 923937.

[12] Sun, H., Xiao, R., Liu, W., and Wang, F., 2013, "Analysis of S Characteristics and Pressure Pulsations in a Pump-Turbine With Misaligned Guide Vanes," ASME J. Fluids Eng., **135**(5), p. 051101.

[13] Li, W., Pan, Z., and Shi, W., 2012, "Numerical Investigation of Pump-Turbines With Different Blades at Pump Conditions," J. Adv. Manuf. Syst., **11**(2), pp. 143–153.

[14] Rodriguez, C. G., Mateos-Prieto, B., and Egusquiza, E., 2014, "Monitoring of Rotor-Stator Interaction in Pump-Turbine Using Vibrations Measured With On-Board Sensors Rotating With Shaft," Shock Vib., **2014**, p. 276796.

[15] Gentner, C., Sallaberger, M., Widmer, C., Barun, O., and Staubli, T., 2012, "Analysis of Unstable Operation of Pump Turbines and How to Avoid It," HYDRO Innovative Approaches to Global Challenges, Bilbao, Spain, Oct. 29–31, pp. 1–10.

[16] Pavesi, G., Cavazzini, G., and Ardizzon, G., 2008, "Time–Frequency Characterization of the Unsteady Phenomena in a Centrifugal Pump," Int. J. Heat Fluid Flow, **29**(5), pp. 1527–1540.

[17] Pavesi, G., Cavazzini, G., and Ardizzon, G., 2008, "Time-Frequency Characterization of Rotating Instabilities in a Centrifugal Pump With a Vaned Diffuser," Int. J. Rotating Mach., **2008**, p. 202179.

[18] Cavazzini, G., Pavesi, G., Ardizzon, G., Dupont, P., Coudert, S., Caignaert, G., and Bois, G., 2009, "Analysis of the Rotor-Stator Interaction in a Radial Flow Pump," La Houille Blanche, Rev. Int. de l'eau, **5**, pp. 141–151.

[19] Yang, J., Pavesi, G., Cavazzini, G., and Yuan, S., 2013, "Numerical Characterization of Pressure Instabilities in a Vaned Centrifugal Pump Under Part Load Condition," IOP Conf. Ser.: Mater. Sci. Eng., **52**(2), p. 022044.

[20] Yang, J., Pavesi, G., Yuan, S., Cavazzini, G., and Ardizzon, G., 2015, "Experimental Characterization of a Pump-Turbine in Pump Mode at Hump Instability Region," ASME J. Fluids Eng., **137**(5), p. 051109.

[21] Deyou, L., Hongjie, W., Gaoming, X., Ruzhi, G., Xianzhu, W., and Zhansheng, L., 2015, "Unsteady Simulation and Analysis for Hump Characteristics of a Pump Turbine Model," Renewable Energy, **77**, pp. 32–42.

[22] Gentner, C., Sallaberger, M., Widmer, C., Braun, O., and Staubli, T., 2012, "Numerical and Experimental Analysis of Instability Phenomena in Pump Turbines," IOP Conf. Ser.: Earth Environ. Sci., **15**(3), p. 032042.

[23] Cavazzini, G., Pavesi, G., and Ardizzon, G., 2011, "Pressure Instabilities in a Vaned Centrifugal Pump," Proc. Inst. Mech. Eng., Part A, **225**(7), pp. 930–939.

[24] Pavesi, G., Cavazzini, G., Yang, J., and Ardizzon, G., 2014, "Flow Phenomena Related to the Unstable Energy-Discharge Characteristic of a Pump-Turbine in Pump Mode," 15th International Symposium on Transport Phenomena and Dynamics of Rotating Machinery (ISROMAC), Honolulu, HI, Feb. 24–28, pp. 1–8.

[25] Pavesi, G., Yang, J., Cavazzini, G., and Ardizzon, G., 2015, "Experimental Analysis of Instability Phenomena in a High-Head Reversible Pump-Turbine at Large Partial Flow Condition," 11th European Conference on Turbomachinery Fluid Dynamics and Thermodynamics (ETC), Madrid, Spain, Mar. 23–27, pp. 1–13.